RESEARCH ARTICLE

A Metallurgical Approach Toward Bloating of Canal-Dredging Sediments

A. Peys[1] · J. Van De Sande[2,3] · P. Teck[1,4] · R. Snellings[1]

Abstract

The similarity of the fine fraction of dredged freshwater sediments to natural clays stimulates the valorization in a product similar to expanded clay aggregates, obtained by bloating at high temperature. The impact of the ratios between different flux elements $(Fe_2O_3 + CaO + MgO + K_2O + Na_2O)$ on the melting behavior is quantified using thermodynamic modeling and validated with experiments. The total content of alkalis is found to be key in controlling melting and bloating. Increased alkali content triggers the formation of alkali feldspars that start to melt at low temperature and give rise to a gradual increase of the amount of melt with temperature. The ratio $(CaO + MgO + K_2O + Na_2O)/Al_2O_3$ should preferably be smaller than or close to 1 to avoid excessive pyroxene formation, which causes complete meltdown of the granules around 1150 °C. The chemical composition has a complex influence on the melting behavior, even when on the same location on the SiO_2–Al_2O_3–flux diagram. The conventional approach of trying to modify the composition towards a certain range in the ternary diagram does not work for all materials, and therefore, the understanding of the melting behavior using the phase composition at high temperature (= the metallurgical approach) provided in this work is shown to be crucial to produce lightweight aggregates from materials with a higher chemical variability.

Graphical Abstract
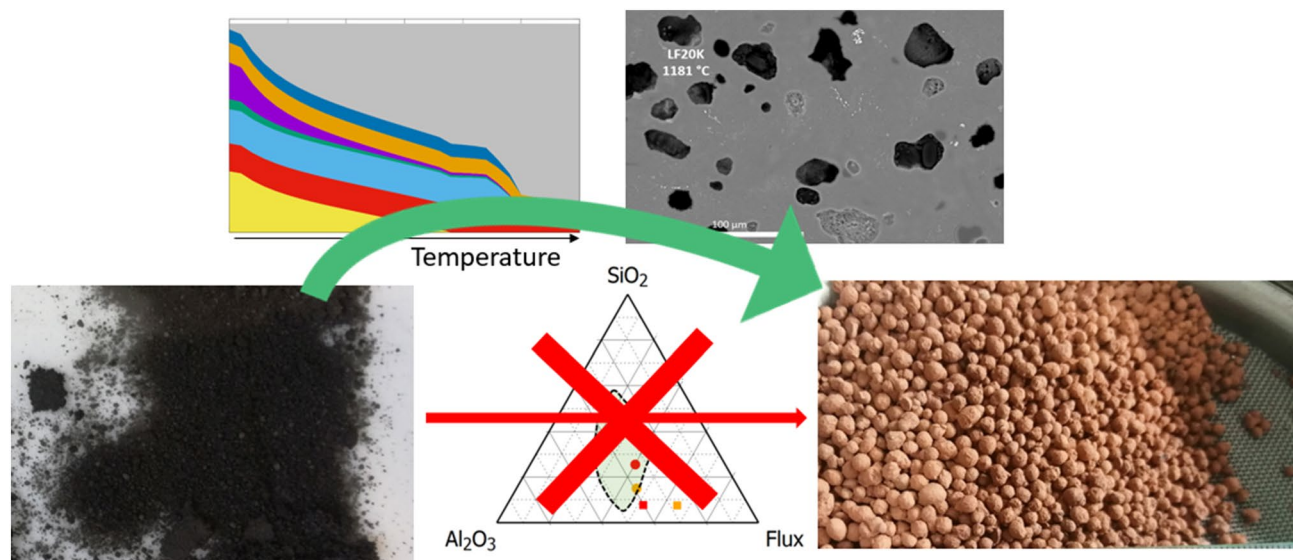
Production of lightweight aggregates from chemically variable raw materials (e.g. dredging sediments):
❌ Ternary diagram and Riley zone do not give enough details
➡ Understanding the phase composition at high temperature enables better understanding

The contributing editor for this article was João António Labrincha Batista

✉ A. Peys
   arne.peys@vito.be

Introduction

In the EU, 50–60 Mt of sediments are dredged from fresh water yearly [1]. More locally, in the 1540 km of waterways in Belgium, 2,400,000 m^3/year is dredged, while in France, 2,800,000 m^3/year is dredged for 8 501 km of waterways [2]. The valorization of these sludges is limited, as only 30% is currently used [1]. The construction of islands, the production of construction materials, and the improvement of soil quality are the main applications. In the construction sector, only the coarse sandy fraction of the dredged sediment is used, while the fine clayey fraction is landfilled or relocated. In the Antwerp harbor alone, 450 kt of fine dredging sediment is landfilled every year [3]. The fine fraction of dredged sediments is often associated with problems related to its organic matter or heavy metal content. The organic matter originates from decaying flora and fauna in the canal, while heavy metals adsorbed to the clay fraction come from industrial activity on or in the vicinity of the canal. The organic fraction can be removed by thermal treatment, while the heavy metals may be immobilized in a solidified matrix. Therefore, calcination of dredging sediments is a potentially suitable way to use the sediment as supplementary cementitious material [3–6]; alternatively, the sediment can be bloated in a rotary kiln to produce lightweight aggregates comparable to expanded clays [7–11].

The production of lightweight aggregates by bloating of clays occurs in a rotary kiln at 1100–1250 °C [12, 13]. During this heating, the feed melts partially, while substances in the clay produce gas. If the melt formation is sufficient in amount and viscosity, the gas is captured and the aggregates expand. The most prominent gas former is Fe_2O_3, although also $CaSO_4$, FeS_2, or organic matter cause gas formation [13, 14]. The melt formation is defined by the chemical composition of the feed. Based on observation of the bloating behavior of a range of chemical compositions [15], Riley [14] proposed a range of suitable bloating compositions in the ternary diagram SiO_2–Al_2O_3–flux (flux = Fe_2O_3 + CaO + MgO + K_2O + Na_2O). This approach has its limitations by not differentiating between the different flux elements. A complementary diagram Al_2O_3–Fe_2O_3–others (others = FeO + CaO + MgO + K_2O + Na_2O) has, therefore, been proposed by Cougny [16] to take into account the significantly different role of Fe_2O_3 in comparison with the Others. The suitable compositional area for lightweight aggregate production in this ternary diagram is dependent on the SiO_2 content. Although this second diagram offers a better representation of bloating behavior, it still ignores the different influences on the melting behavior of Ca, Mg, Na, and K, which are well known in metallurgy to affect the evolution of the phase assemblage and physical properties

of a slag differently with increasing temperature [17–19]. In metallurgy, thermodynamic modeling is, therefore, often used to calculate solidus or liquidus temperatures or to provide an estimation of the mineralogical phase assemblage at a certain temperature, including the quantity of melt phase [20–22]. The application of high-temperature simulations for lightweight aggregate production is not common (yet).

In the production of expanded clay lightweight aggregates, a production facility often sources material from one and the same clay pit for years, reducing variability in chemical composition. This constant source would usually not be available in case when lightweight aggregates would be produced from dredging sediments [7–11]—or waste streams in general [23–29]. In general, dredging sediments have compositions resembling those of natural clays used in lightweight aggregate production and plot within or close to the Riley range in the SiO_2–Al_2O_3–flux ternary diagram. However, dredging sediments generally show larger compositional variability depending on the sources of sediment influx at a specific location (local and river catchment geology, biogenic and anthropogenic sources) [3–11, 30]. This compositional heterogeneity affects organic matter content and ratios of flux elements (e.g., Ca vs. K) to a larger extent than major elements, controlling the phase formation at high temperature, which has a significant influence on the melting behavior [31]. As the Riley range makes abstraction of these variations, it is effectively blind to the technological consequences and is in practice complemented by additional raw meal requirements that are often case or deposit specific. An in-depth study of melting profiles across the Riley diagram using metallurgical modeling enables to rationalize the empirical range proposed, investigate the impact of changes in flux proportions, and potentially propose other compositional ranges suitable for lightweight aggregate production. Confronting the modeling results with experimental melting profiles of actual dredging sediments allows to verify the suitability of the modeling approach and assumptions, and delivers valuable insights into the action of key compositional parameters.

The goal of the present study is to systematically investigate the link between the chemical composition of the dredging sediment and the evolution of the phase assemblage and the percentage of melt phase as a function of temperature using FactSage metallurgical modeling. This gives a thermodynamic background to better understand of the empirically defined Riley range and provides additional insights in the influence of the individual flux elements and their proportioning. As a demonstration, the melt profile is used to find the optimal processing temperature for some specific fluvial dredging sediments. The microstructure and pore shapes are assessed using scanning electron microscopy images. The

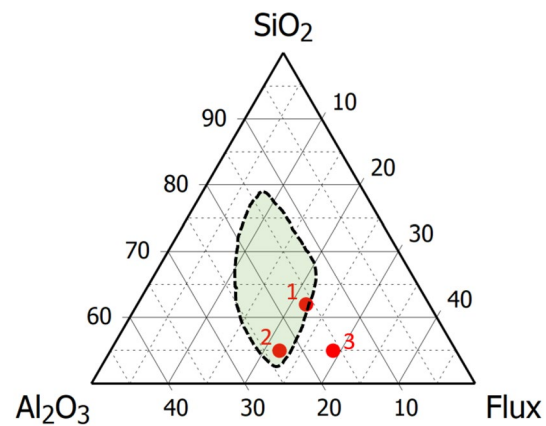**Table 1** Chemical compositions of the model systems

wt.%	SiO$_2$	Al$_2$O$_3$	Fe$_2$O$_3$	CaO	K$_2$O
75Fe25Ca1	62	16	16.5	5.5	0
50Fe50Ca1	62	16	11	11	0
25Fe75Ca1	62	16	5.5	16.5	0
75Fe25K1	62	16	16.5	0	5.5
75Fe25Ca2	55	23	16.5	5.5	0
50Fe50Ca2	55	23	11	11	0
25Fe75Ca2	55	23	5.5	16.5	0
75Fe25K2	55	23	16.5	0	5.5
75Fe25Ca3	55	16	21.75	7.25	0
50Fe50Ca3	55	16	14.5	14.5	0
25Fe75Ca3	55	16	7.25	21.75	0
75Fe25K3	55	16	21.75	0	7.25
50Fe25Ca25K	55	16	14.5	7.25	7.25
75Fe12.5Ca12.5K	55	16	21.75	3.625	3.625
87.5Fe12.5K	55	16	25.375	0	3.625

pore shapes are evaluated quantitatively using image analysis to identify melt phase formation and define the optimal process temperature for bloating.

Materials and Methods

High-Temperature Thermodynamic Modeling

In first instance, virtual model systems with simplified chemical compositions as given in Table 1 are investigated using high-temperature thermodynamic modeling in FactSage. FactSage is a software developed by GTT Technologies, set up in several modules for different types of thermodynamic calculations. The Equilib module of FactSage V 7.3 was used in combination with the FactPS and FToxid databases [32]. This module calculates the equilibrium phase composition at a desired temperature and pressure by a minimization of the Gibbs free energy for the input compositions. The studied model compositions are situated on a SiO$_2$–Al$_2$O$_3$–flux ternary diagram in comparison with the Riley area in Fig. 1 (Flux = Fe$_2$O$_3$ + CaO + MgO + K$_2$O + Na$_2$O). The Riley area was directly taken from the drawings in the paper of Riley [14]. Notice that in the ternary diagram, only 3 different SiO$_2$/Al$_2$O$_3$/Flux ratios are indicated. Keeping the total amount of flux constant, the proportions of the flux elements (Fe$_2$O$_3$, CaO and K$_2$O) are varied as specified in Table 1. The naming of the compositions includes the wt.% of the elements with respect to the total amount of flux and includes an indicator of the point on the ternary phase diagram in Fig. 1. In the sample, 75Fe25Ca1 for example is 75 wt.% of the flux composed of Fe$_2$O$_3$ and 25 wt.% CaO, while the overall composition is located on point 1 in Fig. 1.

Fig. 1 SiO$_2$–Al$_2$O$_3$–flux ternary diagram with indication of the Riley bloating region and the compositions of the model system. Flux = Fe$_2$O$_3$ + CaO + K$_2$O. Values are in wt.%

It should be noted that these systems are not synthesized but only simulated using FactSage modeling, taking advantage of computational efficiency and modularity. From the modeling, the equilibrium phases as function of temperature are obtained. It is assumed that this approximates the actual phase assemblage at high temperature. An oxygen partial pressure of 0.21 atm was imposed corresponding to an oxidizing kiln atmosphere. In the results section, a large number of mineral names was used for the discussion of the results. The supplementary information includes a list of the minerals that are discussed and provides their chemical composition.

Materials

To validate and apply the modeling results, the phase assemblage evolution with temperature of actual dredged sediments from two origins was investigated: the canal Brussels-Charleroi (Belgium, BC) and the canal of Lens (France, LF). The fine fraction < 63 μm is used in both cases. The chemical composition of the two dredged materials (BC and LF) was determined by Kazemi-Kamyab et al. [5] and is shown in Table 2. The numbers do not add up to 100%, mainly because only the carbon content of the organic fraction is displayed, while this fraction consists of more elements than carbon. Results from thermogravimetry and differential scanning calorimetry (TG-DSC) are provided in the supplementary information (Figure S1). More characterization data of the dredging sediments, such as phase composition and particle size distribution, can also be found in the paper of Kazemi-Kamyab et al. [5].

The sediments were used pure and with additions to prepare lightweight aggregates. Additions of fine quartz (SiO$_2$) and kaolinite (Al$_2$Si$_2$O$_5$(OH)$_4$) were made to correct the chemical composition for better bloating. The obtained

Table 2 Chemical composition of dredged sediments by X-ray fluorescence spectroscopy and total carbon (TC) and total organic carbon (TOC) analysis [5]

wt.%	SiO_2	Al_2O_3	Fe_2O_3	CaO	MgO	K_2O	Na_2O	SO_3	P_2O_5	TC	TOC
BC	40.8	13.9	10.0	2.6	1.1	2.1	0.5	1.0	1.1	13.2	12.0
LF	32.2	8.2	4.3	10.8	0.9	1.6	1.9	4.0	1.4	13.8	10.4

Table 3 Calculated chemical composition of the mixtures to produce lightweight aggregates

wt.%	SiO_2	Al_2O_3	Fe_2O_3	CaO	MgO	K_2O	Na_2O	SO_3	P_2O_5
BC	55.8	19.0	13.7	3.6	1.5	2.9	0.7	1.4	1.5
BC10S	61.1	16.7	12.0	3.1	1.3	2.5	0.6	1.2	1.3
LF	49.3	12.6	6.6	16.5	1.4	2.5	2.9	6.1	2.1
LF20K	50.2	18.8	5.4	13.4	1.1	2.0	2.4	5.0	1.7
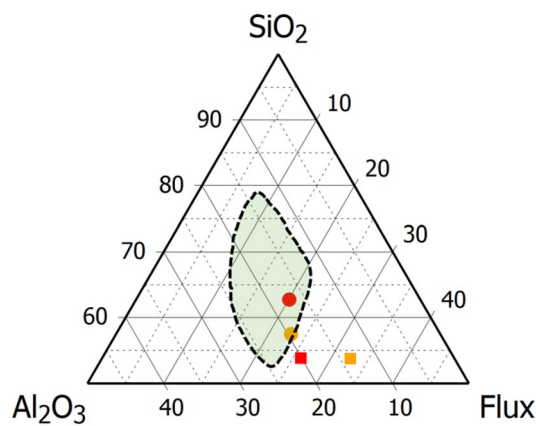
Fig. 2 SiO_2–Al_2O_3–flux ternary diagram with indication of the Riley bloating region and the studied dredging sediment mixtures. Flux = Fe_2O_3 + CaO + MgO + Na_2O + K_2O. Values are in wt.%

mixtures are presented in Table 3. The composition after heat treatment > 800 °C is shown; the carbon content is subtracted and the results are renormalized. The wt.% of sediment replaced by quartz is presented as #S (e.g., BC10S), the wt.% of kaolinite as #K (e.g., LF20K for 20 wt.% of sediment LF replaced by kaolinite).

These mixtures are recalculated to the ternary system SiO_2–Al_2O_3–flux and presented in the ternary diagram in Fig. 2. The raw dredging sediments are indicated in orange, and the mixtures with additions are shown in red. The BC-based mixtures are presented as circles, the LF based as squares. The bloating compositional range determined by Riley [14] is drawn in green with a dashed border. The BC material plots within the Riley range, while the LF materials plot outside due to a higher flux content (higher CaO and Na_2O, but lower Fe_2O_3 than BC).

Experimental Methods

To shape the powders into granules, the mixtures in Table 3 and Fig. 2 were granulated in an Eirich mixer. Demineralized water was added to 500 g of dried powder during mixing at rotor speed 15–20 m/s and pan speed 0.5 m/s until a liquid/solid mass ratio of 0.45 was obtained. Granules were formed by decreasing the rotor speed to 1.5–2 m/s and increasing the pan speed to 1 m/s. Furnace experiments used a Carbolyte tube furnace with a sealed quartz tube. An air flow was applied of 300 ml/min. The heating and cooling rate in all experiments was 5 °C/min, and the temperature was fixed at 1100, 1125, 1150, and 1175 °C for 30 min. The actual temperature during the experiments measured using a thermocouple at the sample location in the furnace was 1121, 1141, 1161, and 1181 °C, respectively. The sediment LF was also treated at 1129 °C, as a more detailed assessment of the required processing temperature was required. Alumina crucibles were used.

X-ray diffraction (XRD) measurements were made on a PANalytical Empyrean with a Co target using 40 kV and 45 mA, step size of 0.0131° 2θ, and cumulative counting time of 0.02 s/step. The analysis was carried with HighScore X'pert software. Quantification was done by Rietveld refinement, and a rutile external standard was used to estimate the amorphous content. The amorphous content is considered as a measure of the amount of melt phase at the processed temperature.

Fired granules were embedded in resin and polished cross section was subjected to a scanning electron microscopy study. For SEM, a platinum/palladium coating was applied. SEM backscattered electron (BSE) images were collected in a FEI Nova NanoSEM 450 using an acceleration voltage of 20 kV. Image analysis used SEM BSE images with a magnification of 250 (HFW 508 µm). These images are processed with OpenCV [33] to identify and segment the

internal pores. Image processing steps consist of applying a bilateral filter smoothing the image, thresholding based on gray level and removing noise in the thresholded binary image. Only pores not in contact with the side of the image were taken into account for further analysis. The shape of the pores was quantified by calculating the solidity (= actual area/convex hull area).

Results and Discussion

High-Temperature Phase Formation in the Model Systems

Fundamental understanding on the melting behavior of compositions close to dredging sediments was gained from studying the model system. The wt.% of melt phase is shown in Fig. 3 and has a distinct evolution for the different flux elements. The graphs in Fig. 3 are grouped by position on the Riley diagram. Figure 3a shows point 1 (highest in SiO_2), Fig. 3b point 2 (highest in Al_2O_3) and Fig. 3c point 3 (highest in flux elements). Figure 3d shows some extra compositions for point 3. A comparison of Fig. 3a–c indicates that the melting behavior is more extensively influenced by the type of flux element than by the position on the ternary diagram, despite the fact that Fig. 3a and b represent compositions in the Riley range and 4c outside of this range. The presence of large amounts of Ca seems to result in an increase in wt.% of melt at 1150 °C, while the presence of K results in melting starting already at 950 °C. The simultaneous presence of Ca and K does not follow a rule of mixture with partial melting at 950 °C and partially at 1150 °C, instead, a melt is obtained from a temperature of 1050 °C. The experiments later in this paper will show that the optimal wt.% of melt phase is approximately 40–50 wt.%. In Fig. 3a–c all samples show a relatively steep increase around these values of wt.% melt, which interferes with the robustness of the production process. Figure 3d shows that by tailoring the chemistry of the system, a more smooth evolution of the wt.% of melt as function of temperature can be obtained, even if these compositions are outside of the Riley range.

The phase composition just below the solidus temperature (T_s) is key to explain the evolution of the wt.% of melt phase. The estimation of this phase composition from the FactSage calculations is provided for all compositions in Table 4. The melting of samples containing only Fe and Ca as flux elements is controlled by the andradite content. A comparison of Table 4 and Fig. 3 shows that the wt.% of andradite is inversely related to the rise in wt.% melt phase around 1150 °C. A more detailed investigation of the FactSage results shows that andradite melts together
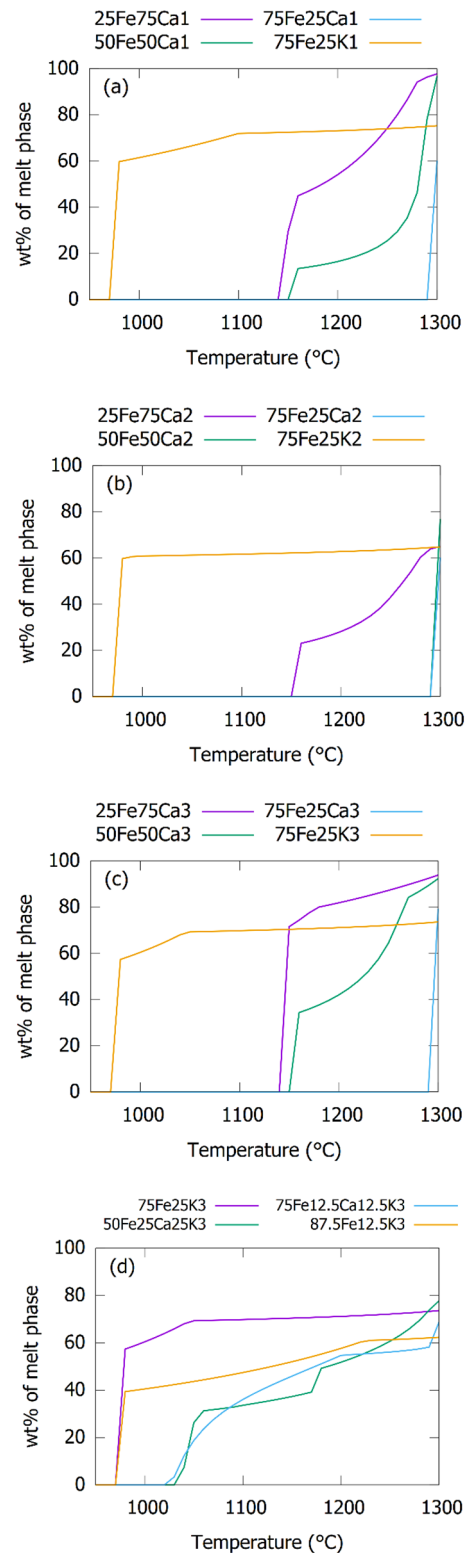
Fig. 3 Quantity of melt phase in wt.% as a function of temperature in the model systems calculated by FactSage

Table 4 Solidus temperatures (T_s) and mineralogical compositions in wt.% 10 °C below T_s

Sample	75Fe25Ca1	50Fe50Ca1	25Fe75Ca1	75Fe25K1	75Fe25Ca2	50Fe50Ca2	25Fe75Ca2	75Fe25K2
T_s (°C)	1300	1160	1150	980	1300	1300	1160	980
Hematite	16.5	8.9	0.0	16.5	16.5	11.0	1.9	16.5
Quartz	48.1	40.8	34.9	37.3	38.6	30.4	23.8	27.8
Andradite	0.0	6.6	17.5	0.0	0.0	0.0	11.5	0.0
Anorthite	27.2	43.7	43.7	0.0	27.2	54.5	62.8	0.0
Orthoclase	0.0	0.0	0.0	32.5	0.0	0.0	0.0	32.5
Wollastonite	0.0	0.0	3.9	0.0	0.0	0.0	0.0	0.0
Mullite	8.2	0.0	0.0	13.6	17.7	4.2	0.0	23.2

Sample	75Fe25Ca3	50Fe50Ca3	25Fe75Ca3	75Fe25K3	50Fe25Ca25K3	75Fe12.5Ca12.5K3	87.5Fe12.5K3
T_s (°C)	1300	1160	1150	980	1040	1030	980
Hematite	21.8	9.1	0.0	21.8	11.9	21.8	25.4
Quartz	38.5	30.0	22.3	24.3	14.6	31.4	36.8
Andradite	0.0	17.1	23.1	0.0	8.3	0.0	0.0
Anorthite	35.9	43.7	43.7	0.0	22.3	17.9	0.0
Orthoclase	0.0	0.0	0.0	42.9	42.9	21.4	21.4
Wollastonite	0.0	0.0	10.9	0.0	0.0	0.0	0.0
Mullite	3.9	0.0	0.0	11.1	0.0	7.5	16.4

with part of the quartz, anorthite, and wollastonite (if present). If wollastonite is present, this happens at 1150 °C, otherwise at 1160 °C. The presence of andradite is controlled by the Ca/Al ratio. As anorthite is more stable than andradite, first anorthite is formed until the system runs out of Al, the rest of the Ca is present in andradite until the system runs out of Fe. Wollastonite is formed when there is still Ca in the system afterwards. This results in melt formation at a higher temperature in systems with a Ca/Al molar ratio < 0.5. Therefore, the samples 75Fe25Ca# and sample 50Fe50Ca2 can only obtain a melt at ≥ 1300 °C. These samples are all mixtures of anorthite, hematite, quartz, and mullite.

The presence of K changes the melting behavior completely. The presence of orthoclase causes melt formation at 980 °C. A closer look at the FactSage data shows that at this temperature, orthoclase has a eutectic point together with quartz, resulting in extensive melting of both phases. The excess of orthoclase or quartz melts gradually above this temperature. This causes for instance that composition 87.5Fe12.5K3 in Fig. 3d shows a steep increase of wt.% melt phase at 980 °C until 40 wt.%, which afterwards slowly increases up to 60 wt.% at 1220 °C.

The melting behavior becomes more complex when Ca and K are present together. As anorthite and orthoclase have similar crystal structures (both feldspars), they are present as solid solutions, i.e., small amounts of K are present in anorthite and Ca in orthoclase. This causes that the presence of Ca stabilizes orthoclase, increasing the solidus temperature and causing that the orthoclase and quartz does

not completely melt at the eutectic temperature of the pure phases. Instead, a more gradual increase in wt.% melt phase is observed. The presence of andradite is limited in these samples, causing no additional step increase in melt content around 1150 °C. The andradite content is now controlled by the molar ratio (K + 2Ca)/Al, as also orthoclase incorporates Al. Sample 75Fe12.5Ca12.5 K still contains mullite, suggesting an excess of Al. This excess of Al seems contradictory to the sample being outside of the Riley range at the low Al side. The above observations can be reformulated as compositional guidelines:

- The evolution of the wt.% of melt phase is more dependent on the flux element type than on the position on the ternary diagram.
- (K + 2Ca)/Al < 1 avoids the formation of andradite and avoids a sudden increase in melt formation around 1150 °C.
- The amount of K should be dosed properly. A small amount is needed to start melt formation early and as such flatten the curve. However, if too much is added, then extensive amount of melt is already formed at low temperatures.

## High-Temperature Phase Formation in the Dredging Sediments

FactSage calculations were also made for the actual dredging sediments from the Brussels-Charleroi (BC) and Lens (LF) canals and the mixtures with additions of fine quartz
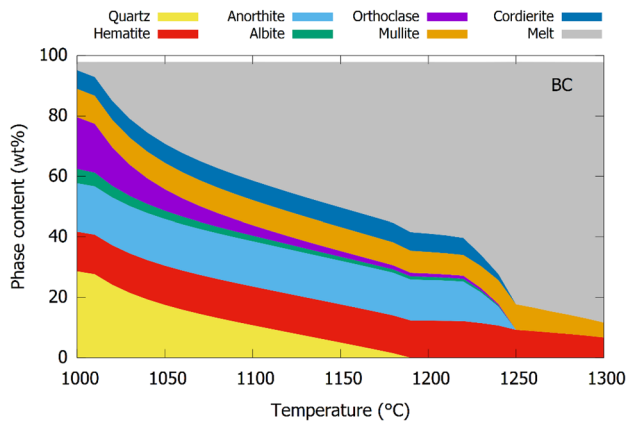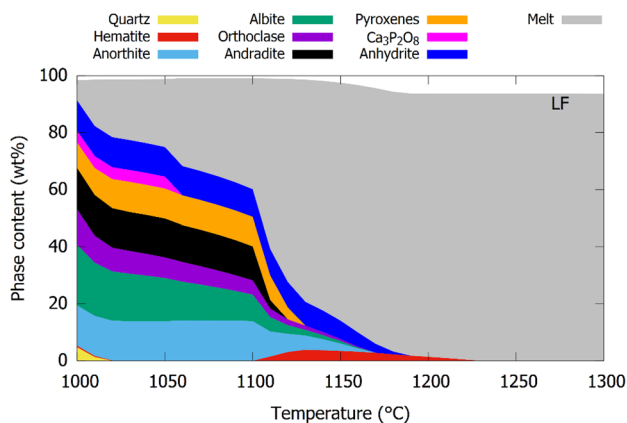
Fig. 4 Phase composition of the BC sediment in the range 1000–1300 °C as calculated by FactSage
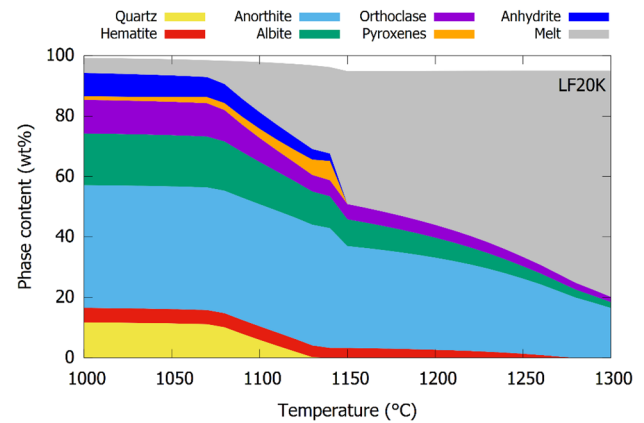
Fig. 7 Phase composition of the LF20K mixture in the range 1000–1300 °C as calculated by FactSage
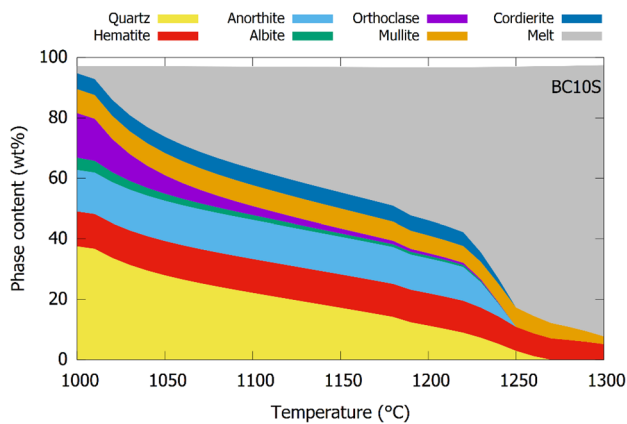
Fig. 5 Phase composition of the BC10S mixture in the range 1000–1300 °C as calculated by FactSage

Fig. 6 Phase composition of the LF sediment in the range 1000–1300 °C as calculated by FactSage

(BC10S) and kaolinite (LF20K). The estimation of the equilibrium phase composition as a function of temperature from 1000 to 1300 °C is shown in Figs. 4, 5, 6, and 7 for the 4 compositions. The total phase content does not add up to 100 wt.% because minor phases (<0.1 wt.%) are not reported in the figures. Looking first at the wt.% of the melt phase, the compositions based on BC dredging sediment show a gradual evolution as function of temperature, especially in the region of 30–60 wt.% melt. In contract, the LF sediment without additions shows a steep increase in wt.% of melt phase from 40 wt.% at 1100 °C to 80 wt.% at 1125 °C. The addition of 20 wt.% of kaolinite would reduce the increase, although the evolution is still more steeper than for the BC mixtures. The decrease in total wt.% in the LF mixtures around 1150 °C is caused by the decomposition of $CaSO_4$ and the emission of SO_3 gas. It is important to mention that after decomposition of $CaSO_4$, the Ca participated in the formation of anorthite and andradite or melt and should thus still be taken into account in calculations (of for instance the $(2Ca + K)/Al$ ratio).

The evolution of the wt.% of melt phase of the BC mixtures in Figs. 4 and 5 is similar to the 75Fe125Ca125K3 model system, and they are also close in chemical composition. The phase assemblage also seems similar. The minor elements in the real dredging sediment adds two mineralogical phases. Na is present in albite, an alkali feldspar like orthoclase. The presence of Mg causes the formation of cordierite. An excess of Al is observed, demonstrated by the presence of mullite. The first melt is produced by the alkali feldspars (albite and orthoclase) and quartz. These phases gradually melt below 1000 °C. Between 1225 and 1250 °C cordierite, anorthite, and the remaining alkali feldspars dissolve into the melt. Above 1250 °C, only hematite and mullite remain solid. As below 1225 °C, the gradual melting of alkali feldspars and quartz is the only melting occurring in

these samples, the evolution of the wt.% of melt phase is also very gradual.

Due to the high Ca content, the LF mixtures do not have excess Al. Even with the addition of 20 wt.% kaolin, no mullite is observed in Figs. 6 and 7. The minor content of Mg, therefore, also does not form cordierite, but the pyroxene phase diopside. The pyroxenes indicated on the graph are mainly a solid solution of diopside and hedenbergite. The presence of S and P leads to the formation of $CaSO_4$ and $Ca_3P_2O_8$, respectively. In LF20K, the phosphate already melted below 1000 °C. The melt formation in LF is predicted to initiate by melting of the alkali feldspars and a minor amount of quartz. The alkali feldspars melt gradually until 1100 °C. At 1050 °C, the phosphate phase melts in LF. Between 1100 and 1125 °C, andradite and pyroxenes are melting completely, also speeding up the melting of the remaining feldspars. This acceleration of the melting of the feldspars is caused by the change in melt composition, shifting the equilibrium. This behavior is strongly changed by the addition of 20 wt.% of kaolinite. The presence of a high amount of anorthite stabilizes the alkali feldspars—the composition moves more towards anorthite with a solid solution of Na and K, rather than a combination of anorthite and alkali feldspars. Therefore, melting of the alkali feldspars and quartz only starts from 1075 °C. Quartz melts completely by 1125 °C. The alkali feldspars melt gradually, even at 1300 °C, a minor amount is still present. Between 1125 and 1150 °C, the pyroxenes and $CaSO_4$ melt. This causes a quite steep increase in melt phase from 1075 °C (5 wt.% melt) to 1150 °C (50 wt.% melt).

The simulation results on the actual dredging sediments confirm that the presence of sufficient Al is important to avoid the presence of andradite, which causes extensive melting at 1100–1125 °C. Similarly, the Mg content should be limited or compensated with extra Al to avoid the presence of a large amount of pyroxenes, which also melt around 1125 °C. The Ca/alkali ratio in the feldspars is very important to estimate the initial melt formation at 1000–1100 °C. The high Ca/alkali ratio in LF20K hinders the formation of melt phase at 1000–1100 °C, resulting in a more steep increase in wt.% melt, while in the BC mixtures, the alkali feldspars and quartz produce already 30 wt.% melt phase at 1100 °C and a gradual increase of wt.% melt up to approximately 55 wt.% at 1225 °C.

Validation of the Simulations and Optimization of the Process

High-temperature bloating experiments were made to validate the simulations and find the optimal process temperature for producing lightweight aggregates from the dredging sediments. A practical limit to the process temperature that was observed was the fusion of the granules to the alumina crucibles. When this fusion occurred, too much melt had formed and the temperature was evaluated as too high. The mixtures BC, BC10S, and LF20K showed the same maximum process temperature. At 1181 °C, the granules became sticky, but it was still possible to take them out of the crucibles. The LF-dredging sediment was irreversibly fused to the crucible at 1141 °C, and the granules completely collapsed at 1161 °C.

The sintered aggregates that could be recovered from the crucibles were investigated using SEM BSE on polished cross sections. The images in Figs. 8, 9, 10, and 11 show the microstructure of the dredging sediment mixtures as a function of temperature. The roundness and variability in pore size are used to assess whether sufficient melt had formed to facilitate bloating. For a selection of mixtures, images with higher magnification are shown in Fig. 12 to better compare the pore shapes and sizes. The BC mixtures in Fig. 8 and 9 show an increasing pore size with temperature. The roundness of the pores is best observed in Fig. 12, where it can be seen that already at 1141 °C, the pores were relatively round, although Figs. 8 and 9 show that they were still small (≤ 20 μm). The amount of pores and thereby the overall porosity are not considered in this paper. Although the porosity is an important property of lightweight aggregates, the authors do not claim to have obtained products with sufficient porosity. The pore shape and size are merely used to discuss the melting behavior and assess what temperature causes sufficient melt formation to transform irregularly shaped holes to rounded bubbles.

The LF sediment treated at 1129 °C in Fig. 10 showed small and irregular pores. Insufficient melt was obtained at 1129 °C, while at 1141 °C, the aggregates stuck to the crucible. Therefore, there appears to be no temperature window for production of lightweight aggregates. The pores in Fig. 11 and 12 in the granules of mixture LF20K at 1181 °C seem round. This temperature was also the maximum process temperature of this mixture. The temperature window for processing LF20K is, thus, relatively small.

To more quantitatively interpret the textures observed by SEM, image analysis is carried out. The shape of the pores is the main aspect that can help estimate the melting behavior. The formation of sufficient melt for bloating can be assessed by the roundness or convexity of the pore, which indicates when the pore changes from "hole" to "bubble." The solidity (= actual area/convex hull area) was the pore shape parameter that showed the most clear trend and is, therefore, used in the discussion here. The solidity of the pores is calculated for all samples. An example histogram is given in Fig. 13 for the BC sediment, histograms for the other compositions are provided in the supplementary information (Supplementary Figures S2–S4). These histograms confirm the qualitative discussion of the SEM images. From the histograms, the percentage of pores with a solidity higher than 0.9 can be
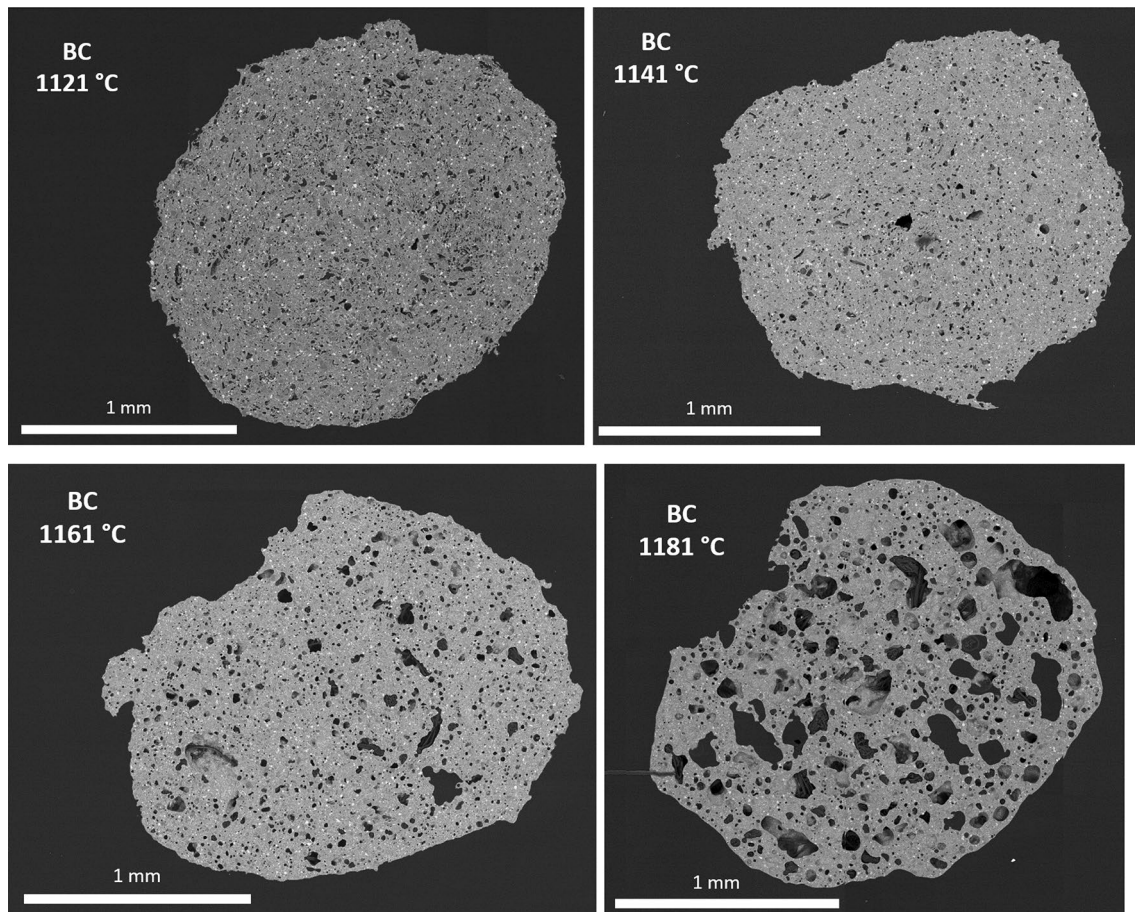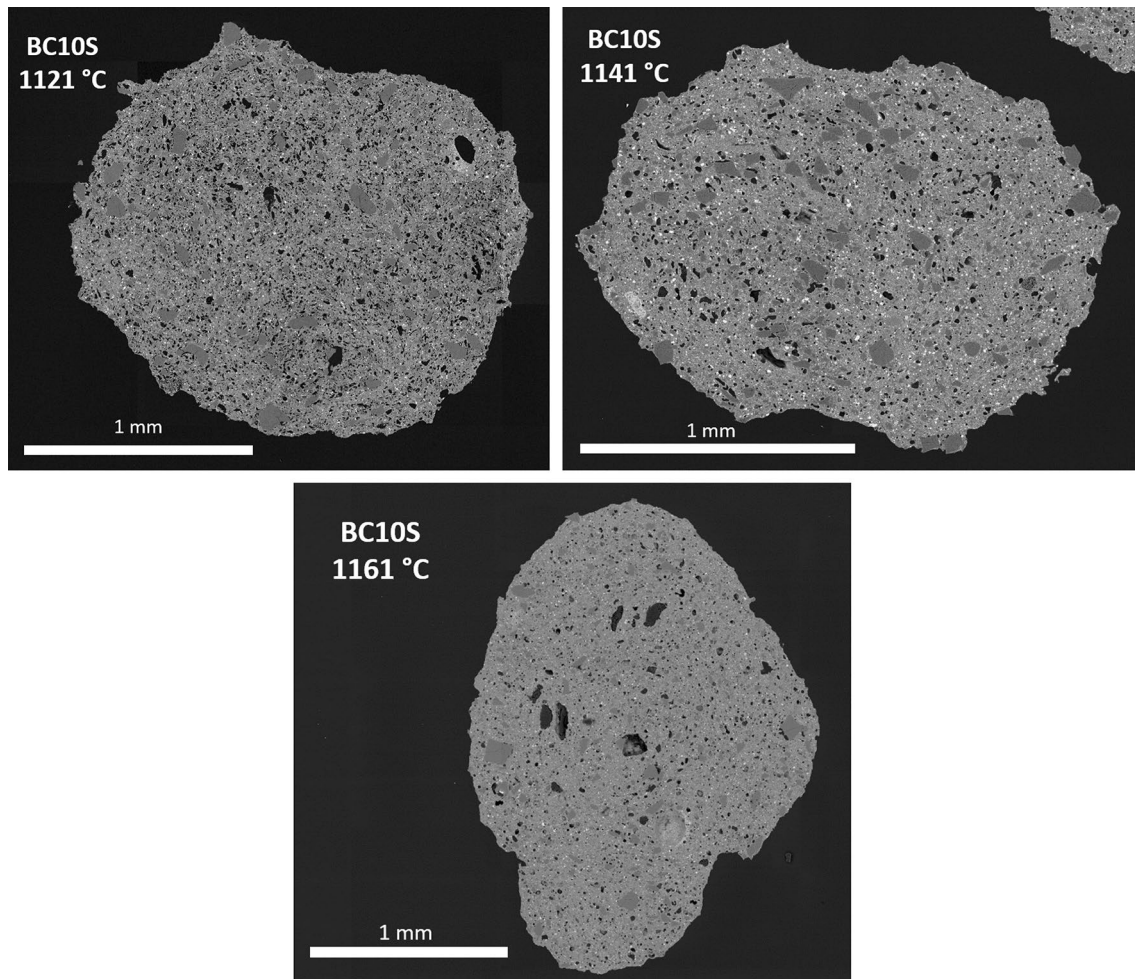
Fig. 8 SEM images of BC after heating to 1121, 1141, 1161, and 1181 °C

calculated to provide a more quantitative comparison. These are round, convex pores which can be seen as bubbles and, therefore, a suitable measure of melt formation. This percentage is plotted for the different mixtures as a function of temperature in Fig. 14. It shows that a percentage of this parameter higher than 40 corresponds to images in which the pores are of sufficient roundness, while the images with a high irregularity result in approximately 30% of pores with a solidity higher than 0.9. As such, the image analysis quantitatively confirms that

- Sediment BC has relatively round pores from 1141 °C, which increase further in solidity at 1161 and 1181 °C.
- Mixture BC10S has a similar evolution of the solidity as sediment BC, but a lower solidity than BC is observed at 1161 °C.
- Sediment LF does not form sufficient melt at 1129 °C to form pores with high solidity.
- Mixture LF20K needs a temperature of at least 1181 °C to increase the solidity of the pores.

The observations from the experiments are summarized in Table 5 to define the temperature window to produce lightweight aggregates. In line with the thermodynamic simulations, a wide temperature window for processing the BC sediment and BC10S mixture is observed. The sudden melting of the LF sediment was expected from modeling as well as the small temperature window for processing the mixture LF20K. However, the temperature at which sudden melting occurred in LF was higher than modeled: 1129–1141 °C instead of 1100–1125 °C. A more detailed comparison between experiments and simulations is needed to explain this.

An assessment of the accuracy of the FactSage simulations is made by comparing the simulated phase compositions with phase compositions of the sintered aggregates determined with XRD analysis. In general, Figs. 15 and 16 show that the FactSage calculations correspond well to the XRD results. Minor deviations occur. In the BC10S mixture, Mg was expected to be present in cordierite; however, the XRD results show that Mg is rather present in an $Mg(Al,Fe)_2O_4$ spinel phase. The evolution of the content of these phases as a function of temperature seems to be similar

Fig. 9 SEM images of BC10S after heating to 1121, 1141, and 1161 °C

and as such the melting behavior is not extensively impacted. The content of mullite seems to be lower than expected, this is in line with the presence of the spinel phase, which
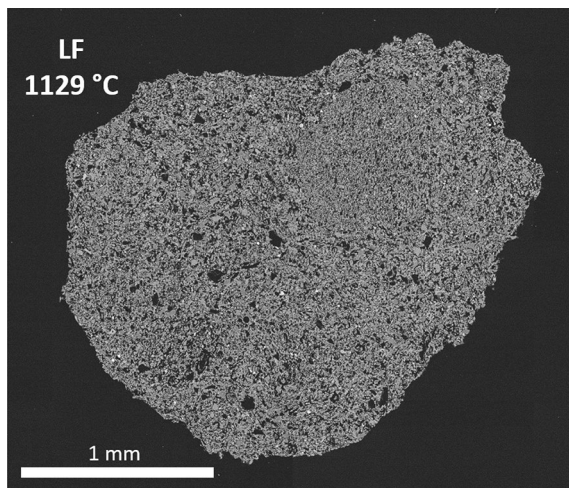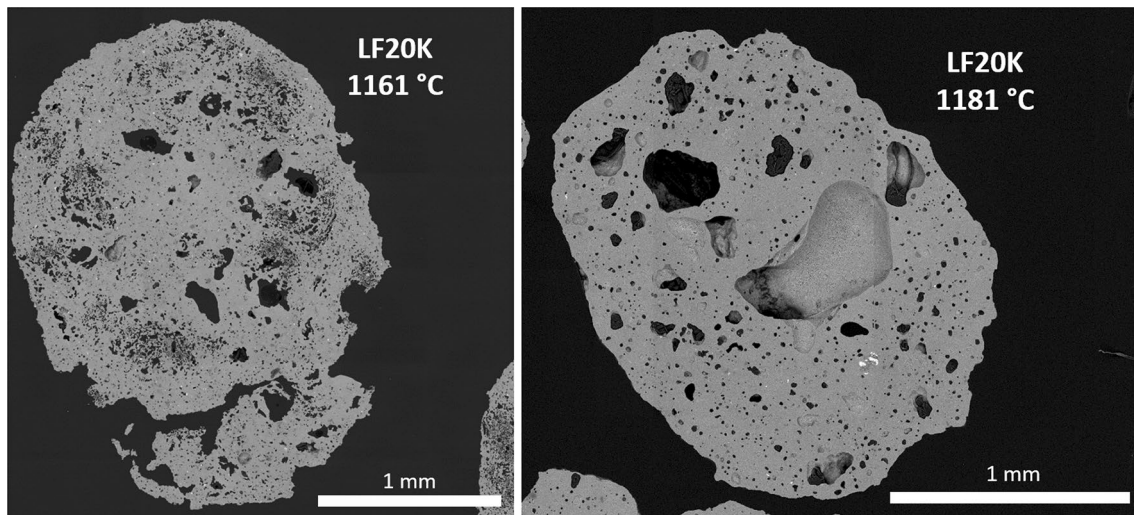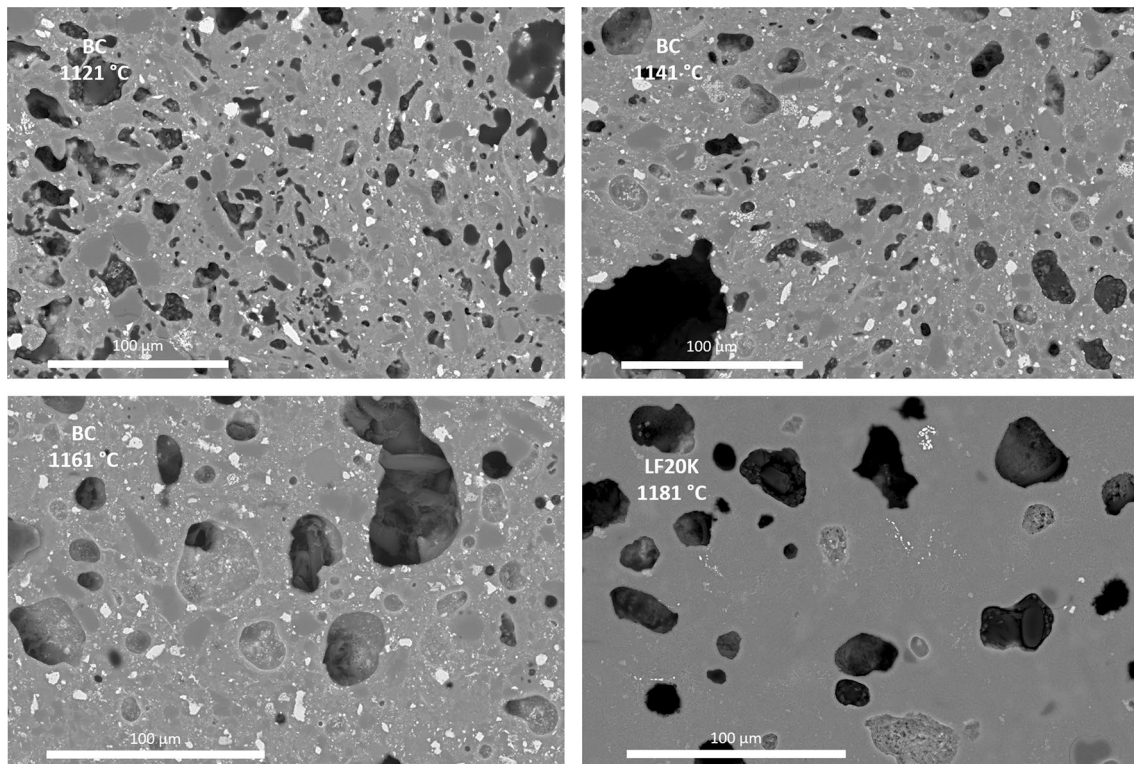

Fig. 10 SEM images of LF after heating to 1129 °C

contains proportionally more Al than cordierite. The larger amount of melt at 1120 °C and 1180 °C in the XRD analysis of the BC10S mixture goes together with a lower feldspar and quartz content. The alkali feldspars are less stabilized by the presence of anorthite than expected from FactSage. However, also the XRD results should be interpreted with care since crystallization of the melt may occur to some extent during cooling. For instance, the result of LF20K at 1180 °C (Fig. 17) shows ~40 wt.% of melt and BC10S at 1120 °C (Fig. 15) ~50 wt.%, while the experiments showed that LF20K at 1180 °C was more sticky and had a rounder pore shape than BC10S at 1120 °C.

An important difference between the simulations and the XRD results was found for the LF-dredging sediment as shown in Fig. 16. No andradite was detected by XRD, instead pyroxenes and wollastonite were identified. The drastic increase in melt phase was observed as simulated (Table 5). XRD results show that the melt formation is only caused by pyroxenes instead of the combination of andradite and pyroxenes. Because pyroxenes melt at a slightly higher

**Fig. 11** SEM images of LF20K after heating to 1161 and 1181 °C

Fig. 12 Higher magnification SEM images of BC after heating to 1121, 1141, and 1161 °C and LF20K after heating to 1181 °C

temperature than andradite, this would explain the shift in temperature of the collapse of the granules with respect to the expected melting temperature and the shift in temperature between the phase assemblages obtained by XRD and FactSage. Therefore, the XRD results on the LF-dredging sediment from the experiments at 1121 °C are more similar to the FactSage data of 1100 °C than to those of 1120 °C.

Slight deviations between experiments and simulations are also observed for the LF20K mixture in Fig. 17. XRD analysis showed that anhydrite was not present in significant amounts at 1120 °C. This is probably due to the evaporation of SO_3 before CaO is available (e.g., decomposition of sulfide minerals before decarbonation of limestone). A lower amount of hematite and anorthite
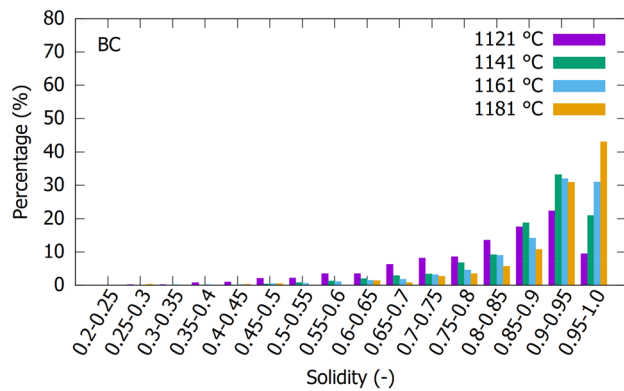
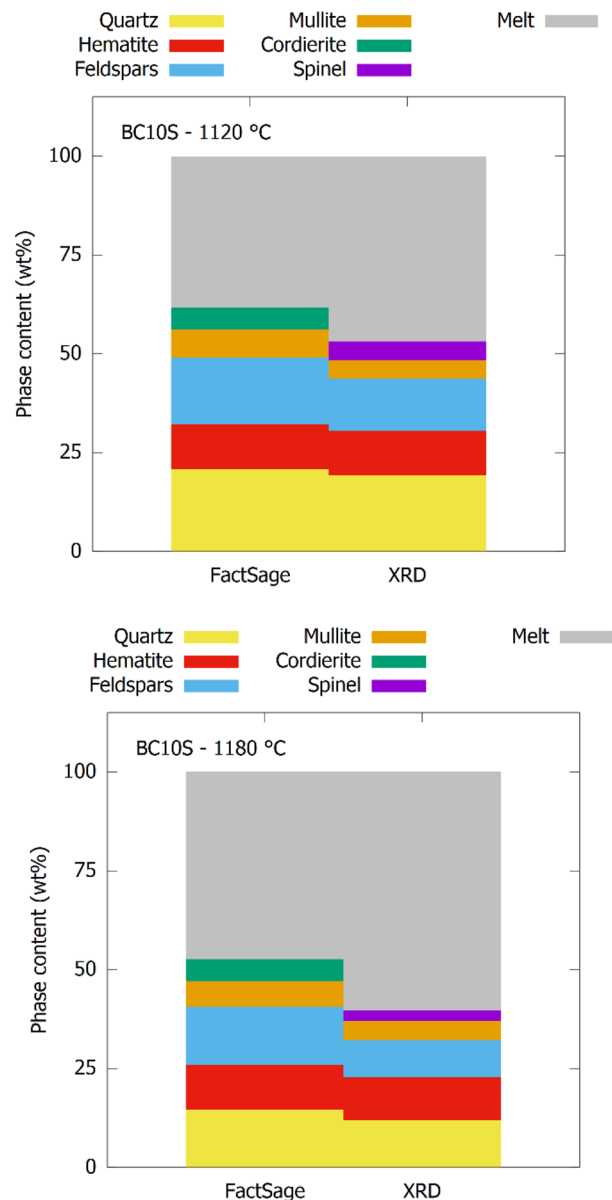**Fig. 13** Pore solidity histogram of the BC sediment at 1121–1181 °C
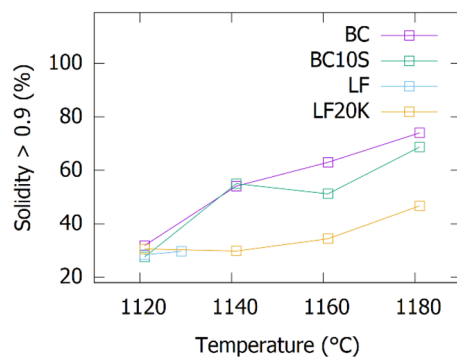
Fig. 14 Percentage of pores with a solidity higher than 0.9 as a function of temperature

Table 5 Qualitative assessment of the melting behavior of the studied mixtures

	1121 °C	1129 °C	1141 °C	1161 °C	1181 °C
BC		/			Sticky
BC10S		/			Sticky
LF			Fused	melts	
LF20M		/			Sticky

Color code: white = insufficient melt, light green = might be sufficient, green = good, red = too much melt (Color figure online)

Fig. 15 Phase composition of the BC10S mixture after heating to 1120 and 1180 °C as calculated with FactSage and measured with XRD

and higher amount of pyroxenes show that more Fe^{3+} is reduced to Fe^{2+} and more Fe and Ca are incorporated in pyroxene phases. Due to the fixed oxygen partial pressure of 0.21 atm, Fe was completely in the Fe^{3+} state in the crystalline phases in the simulations. The conditions during the experiments were, thus, slightly more reducing than the simulated environment. The underestimation of the melt at 1120 °C seems in line with the observations for BC10S and is here probably also associated with the overestimated ability of anorthite to stabilize the alkali feldspars. On the other hand, at 1180 °C in the LF20K mixture, the amount of melt seems to be overestimated.

It seems that the remaining feldspars (mostly anorthite) are not as affected by the alkali content of the mixture. However, as suggested before, the absolute amounts of the phases need to be interpreted cautiously.

Overall the simulations and the experimental observations are in good agreement. The minor differences are summarized as follows:

- Andradite was not found present in any of the mixtures, and pyroxenes were identified instead. These have similar
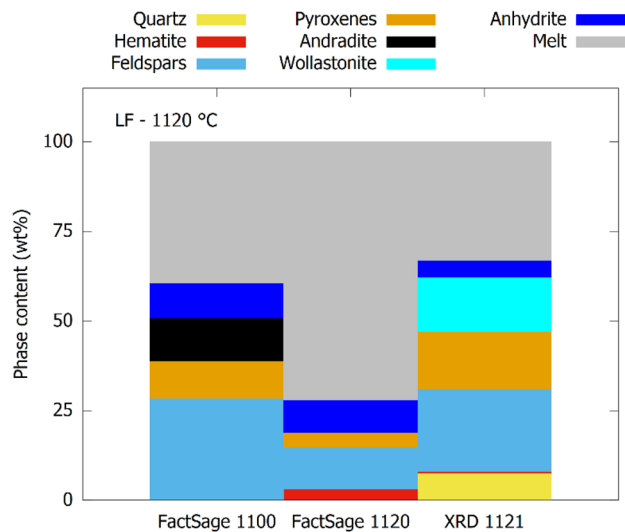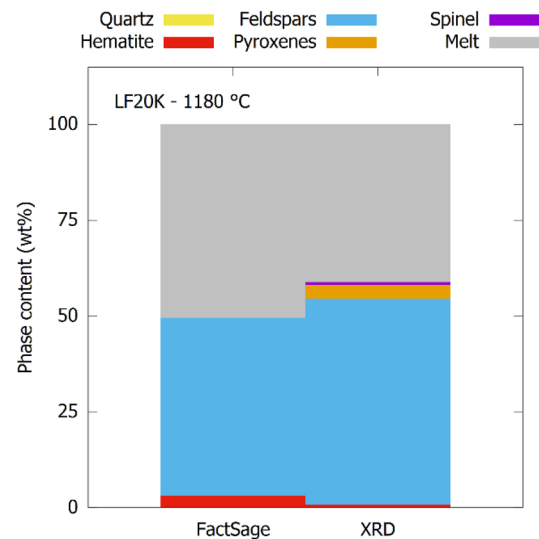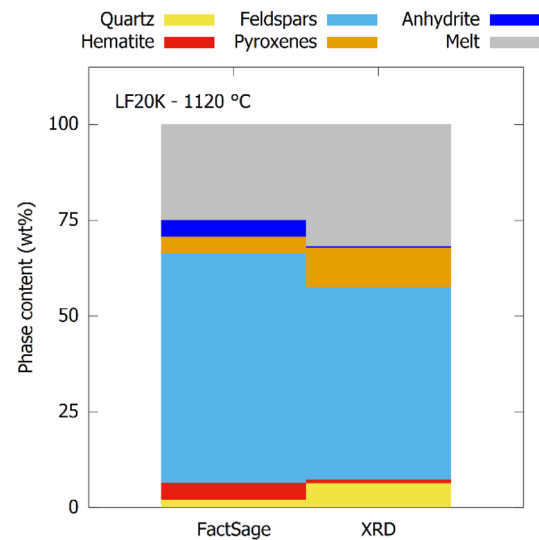
Fig. 16 Phase composition of the LF sediment after heating to 1120 °C as calculated with FactSage and measured with XRD. The phase composition at 1100 °C calculated with FactSage is added as comparison

Fig. 17 Phase composition of the LF20K mixture after heating to 1120 and 1180 °C as calculated with FactSage and measured with XRD

melting behavior, and dissolution in the melt occurs at 1129–1141 °C (instead of 1100–1125 °C for andradite).

- Cordierite was not found present in any of the mixtures, and Mg was present in spinel (sufficient Al) or pyroxene (Al-deficient) phases. This does not impact the melting behavior significantly.
- Pyroxenes contained more Fe than simulated, resulting in less hematite. This is caused by the more reducing environment of the experiments in comparison with the simulations at $pO_2 = 0.21$ atm.
- The melting behavior of alkali feldspars is less affected by the anorthite content than expected from the simulations, due to a lower extent of solid solution. However, the presence of anorthite still delayed the melting of the alkali feldspars.

Recommendations for Bloating

The results in this paper can be summarized as recommendations for the composition of the feed for lightweight aggregates production. A sufficient amount of alkalis needs to be present to initiate melting and provide sufficient melt (> 40 wt.%) at a relatively low temperature (< 1200 °C). As quartz melts together with the alkali feldspars, there is a minimum Si content to achieve sufficient melt formation. To avoid excessive melting (> 60 wt.% melt), there is also a maximum amount of alkalis. It is not possible to provide a number with respect to the maximum and minimum amount of alkalis and the minimum Si content, as they are interrelated and influenced by the Ca content. The Ca and Mg contents should be limited to have a (2Ca + 2 Mg + Na + K)/Al molar ratio < 1

and avoid the extensive formation of pyroxenes, which melt suddenly around 1129–1141 °C. The Ca/(Na + K) ratio also needs to be limited in order not to stabilize the alkali feldspars too extensively. This limit ratio is again interrelated in a complex way with the total alkali content, the Si content, and the (2Ca + 2 Mg + Na + K)/Al ratio. From the perspective of being able to form sufficient melt, there is also a maximum $SiO_2 + Al_2O_3 + Fe_2O_3$, which is directly derived from the minimum alkali content.

The work in this paper only takes into account the melting behavior and a disclaimer that that is the only important factor for the production of lightweight aggregates is provided in this paragraph. The formation of gasses and identification and dosing of the gas forming compounds are

important as well [14]. For dredging sediments, the presence and the amount of organic matter are important with respect to gas formation [11]. In addition, problems can occur when upscaling of the process. The parameter–property relations cannot be directly extrapolated from a laboratory box furnace to a rotary kiln [26, 34], and additional attention needs to go to the heating and cooling rate of the granules [35]. Future work will focus to resolve these aspects for lightweight aggregates from canal dredging sediments. It is also important to note that only Fe in the 3 + oxidation state is considered in the present study, and simulations and experiments were performed applying an oxygen partial pressure of 0.21 atm (= air). The reduction of the oxygen partial pressure will stimulate the reduction of Fe and thereby increase the potential formation of pyroxenes. This should be explored in future work as well.

Conclusions

For the production of lightweight aggregates from canal dredging sediments, it is important to know the melting behavior of the sediment. This paper shows that the melting behavior is dependent on the chemical composition, not only defined by the ternary diagram SiO_2–Al_2O_3–flux (flux = Fe_2O_3 + CaO + MgO + Na_2O + K_2O) but also by the ratios between flux elements. For the compositions studied in this paper, the ratio between flux elements even had a larger impact on the melting behavior than the position on the ternary diagram. The content of alkalis is key in the formation of alkali feldspars, which initiate melting at relatively low temperatures. The melting of these alkali feldspars is mitigated by the presence of a large amount of anorthite (Ca-feldspar), which stabilizes the alkali feldspars by forming solid solutions. The presence of pyroxene minerals (diopside or hedenbergite) at high temperature causes a drastic increase in melt formation around 1150 °C, which interferes with process robustness. The formation of pyroxene minerals is associated with a molar ratio (2Ca + 2 Mg + Na + K)/ Al > 1 in the feed.

Dredging sediment from the canal of Brussels-Charleroi has a suitable composition for bloating, with and without the addition of SiO_2. The alkali content was sufficient to produce a significant amount of melt at low temperatures, and the Al content was sufficient to avoid extensive pyroxene formation and the amount of Ca was limited, avoiding significant stabilization of the alkali feldspars. The composition of the dredging sediment from the canal of Lens does not have a suitable composition for bloating. The Al content is low, resulting in a large amount of pyroxene phases and drastic melting at 1129–1141 °C. The addition of kaolinite corrected the Al content. However, the high Ca/(Na + K) ratio caused a significant stabilization of the alkali feldspars.

This resulted in a steeper increase of the amount of melt with temperature. These foundations were validated by the analysis of pore shapes using SEM and image analysis. From a quantitative comparison of the pore solidity, the Brussels-Charleroi sediment showed bubble-shaped pores from 1141 °C, without having problems with fusion to the crucible at high temperature until 1181 °C. The expected low suitability for bloating of the Lens sediment was confirmed by the absence of bubble-shaped pore up to 1129 °C and collapse of the granule at 1141 °C.

Using the knowledge on the high-temperature phase formation during bloating, it was possible to provide more details on the compositions in the ternary SiO_2–Al_2O_3–flux diagram which can be used for bloating. In fact, a more detailed knowledge beyond the location on the ternary diagram is needed to completely understand the melting behavior. A better view on the possibilities for different compositions and the necessary additions is obtained in comparison with the state of the art, with more flexibility towards the use of residues and dredging sediments from various sources.

Declarations

Conflict of interest The authors declare that they have no conflict of interest.

References

1. European Dredging Association (2005) Dredged Material & Environmental Regulation in EU. European-dredging.eu/Publications. Accessed August 2020
2. Henry M, Brequel H, Meerseman J, Lemiere B (2019) Mineral processing techniques dedicated to the recycling of river sediments to produced raw materials for construction sector. In: Proceedings of the 11th SedNet Conference, Dubrovnik, Croatia, April 2019
3. Snellings R, Cizer O, Horckmans L, Durdzinski PT, Dierckx P, Nielsen P, Van Balen K, Vandewalle L (2016) Properties and pozzolanic reactivity of flash calcined dredging sediments. Appl Clay Sci 129:35–39
4. Benzerzour M, Amar M, Abriak N (2017) New experimental approach of the reuse of dredged sediments in a cement matrix by physical and heat treatment. Constr Build Mater 140:432–444
5. Kazemi-Kamyab H, Van den Abeele L, Henry M, Haouche L, Snellings R (2019) Evaluation of calcined dredged sediments as supplementary cementitious materials. In: Proceedings of the 2nd International Conference of Sustainable Building Materials, 12–15 August 2019, Eindhoven, The Netherlands
6. Amar M, Benzerzour M, Kleib J, Abriak N (2021) From dredged sediment to supplementary cementitious

material: characterization, treatment, and reuse. Int J Sedim Res 36(1):92–109

7. Hung M, Hwang C (2007) Study of fine sediments for making lightweight aggregate. Waste Manage Res 25:449–456

8. Wei Y, Yang J, Lin Y, Chuang S, Wang HP (2008) Recycling harbor sediment as lightweight aggregate. Mar Pollut Bull 57:867–872

9. Wang H (2009) Durability of self-consolidating lightweight aggregate concrete using dredged silt. Constr Build Mater 23:2332–2337

10. Tang C, Chen H, Wang S, Spaulding J (2011) Production of synthetic lightweight aggregate using reservoir sediments for concrete and masonry. Cement Concr Compos 33:292–300

11. Chen H, Yang M, Tang C, Wang S (2012) Production of synthetic lightweight aggregates from reservoir sediments. Constr Build Mater 28:387–394

12. Huybrechts D, Meynaerts E, Van Hoof V, Hooyberghs E, Vrancken K (2008) Beste Beschikbare Technieken (BBT) voor de kleiverwerkende nijverheid. Academia Press, Gent

13. Decleer J, Viaene W (1993) Rupelian Boom clay as raw material for expanded clay manufacturing. Appl Clay Sci 8:111–128

14. Riley CM (1951) Relation of Chemical Properties to the Bloating of Clays. J Am Ceram Soc 34(4):121–128

15. Conley JE, Wilson H, Klinefelter TA (1948) Production of lightweight concrete aggregates from clays, shales, slates, and other materials. Technical report for the US Department of the Interior and Bureau of Mines.

16. Cougny G (1990) Specifications for clayey raw materials used to produce expanded lightweight aggregates. Bull Int Assoc Eng Geol 41:47–55

17. Battle TP, Hager JP (1990) Viscosities and activities in lead-smelting slags. Metall Trans B 21:501–510

18. Mills KC (1993) The influence of structure on the physico-chemical properties of slags. ISIJ Int 33(1):148–155

19. Jak E, Hayes PC, Lee H (1995) Improved methodologies for the determination of high temperature phase equilibria. Met Mater 1:1–8

20. Tripathi G, Malfliet A, Blanpain B, Guo M (2019) Dissolution behavior and phase evolution during aluminum oxide dissolution in BOF slag. Metall and Mater Trans B 50:1782–1790

21. Chen L, Malfliet A, Jones PT, Blanpain B, Guo M (2019) Influence of Al_2O_3 level in CaO–SiO_2–MgO–Al_2O_3 refining slags on slag/magnesia-doloma refractory interactions. Metall and Mater Trans B 50:1822–1829

22. Schupsky JP, Guo M, Blanpain B, Müller M (2020) The impact of sample homogeneity, crucible material, and oxygen partial pressure on the crystallization of Fe-rich oxidic slag in CSLM experiments. J Sustain Metall 6:216–226

23. Cheeseman CR, Virdi GS (2005) Properties and microstructure of lightweight aggregate produced from sintered sewage sludge ash. Resour Conserv Recycl 45:18–30

24. Mueller A, Sokolova SN, Vereshagin VI (2008) Characteristics of lightweight aggregates from primary and recycled raw materials. Constr Build Mater 22:703–712

25. Chiou I, Wang K, Chen C, Lin Y (2006) Lightweight aggregate made from sewage sludge and incinerated ash. Waste Manage 26:1453–1461

26. Cheeseman CR, Makinde A, Bethanis S (2005) Properties of lightweight aggregate produced by rapid sintering of incinerator bottom ash. Resour Conserv Recycl 43:147–162

27. Cunning PJ, Hills CD, Carey PJ (2009) Production of lightweight aggregate from industrial waste and carbon dioxide. Waste Manage 29:2722–2728

28. Yang C, Cui C, Qin J (2015) Recycling of low-silicon iron tailings in the production of lightweight aggregates. Ceram Int 41(1B):1213–1221

29. Chuang K, Lu C, Chen J, Wey M (2018) Reuse of bottom ash and fly ash from mechanical-bed and fluidized-bed municipal incinerators in manufacturing lightweight aggregates. Ceram Int 44(11):12691–12696

30. Ennahal I, Maherzi W, Benzerzour M, Mamindy Y, Abriak N (2020) Performance of lightweight aggregates comprised of sediments and thermoplastic waste. Waste Biomass Valorization. https://doi.org/10.1007/s12649-020-00970-1

31. Moreno-Maroto JM, Gonzalez-Corrochano B, Alonso-Azcarate J, Rodriguez L, Acosta A (2018) Assessment of crystalline phase changes and glass formation by Rietveld-XRD method on ceramic lightweight aggregates sintered from mineral and polymeric wastes. Ceram Int 44(10):11840–11851

32. Bale CW, Bélisle E, Chartrand P, Decterov SA, Eriksson G, Gheribi AE, Hack K, Jung IH, Kang YB, Melançon J, Pelton AD, Petersen S, Robelin C, Sangster J, Spencer P, Van Ende MA (2016) FactSage thermochemical software and databases, 2010–2016. Calphad 54:35–53

33. Bradski G (2000) The opencv library. Dr Dobb's J Software Tools 25:120–125

34. Bernhardt M, Tellesbø H, Justnes H, Wiik K (2013) Mechanical properties of lightweight aggregates. J Eur Ceram Soc 33(13–14):2731–2743

35. Bernhardt M, Tellesbø H, Justnes H, Wiik K (2014) The effect of heat treatment and cooling rate on the properties of lightweight aggregates. J Eur Ceram Soc 34(5):1353–1363

Authors and Affiliations

A. Peys[1] · **J. Van De Sande[2,3]** · **P. Teck[1,4]** · **R. Snellings[1]**

[1] Sustainable Materials Management, VITO, Boeretang 200, 2400 Mol, Belgium

[2] Department of Materials and Chemistry, Vrije Universiteit Brussel, Pleinlaan 2, 1050 Brussels, Belgium

[3] KU Leuven Department of Materials Engineering, Kasteelpark Arenberg 44, 3001 Leuven, Belgium

[4] KU Leuven Department of Earth and Environmental Sciences, Celestijnenlaan 200E, 3001 Leuven, Belgium